Andrew Honeycutt
Department of Mechanical Engineering
and Engineering Science,
University of North Carolina at Charlotte,
9201 University City Boulevard,
Charlotte, NC 28223
e-mail: ahoney15@uncc.edu

Tony L. Schmitz[1]
Mem. ASME
Department of Mechanical Engineering
and Engineering Science,
University of North Carolina at Charlotte,
9201 University City Boulevard,
Charlotte, NC 28223
e-mail: tony.schmitz@uncc.edu

Surface Location Error and Surface Roughness for Period-*N* Milling Bifurcations

This paper provides time domain simulation and experimental results for surface location error (SLE) and surface roughness when machining under both stable (forced vibration) and unstable (period-2 bifurcation) conditions. It is shown that the surface location error follows similar trends observed for forced vibration, so zero or low error conditions may be selected even for period-2 bifurcation behavior. The surface roughness for the period-2 instability is larger than for stable conditions because the surface is defined by every other tooth passage and the apparent feed per tooth is increased. Good agreement is observed between simulation and experiment for stability, surface location error, and surface roughness results. [DOI: 10.1115/1.4035371]

Keywords: milling, dynamics, chatter, bifurcation, surface location error, surface roughness

Introduction

Research in machining dynamics and instability has spanned over seven decades. In 1946, Arnold analyzed tool vibration during steel machining [1]. Follow-on work used time-delay differential equations to describe the self-excited vibrations (chatter) that can occur when machining [2], identified regeneration of surface waviness from one revolution (turning) or tooth (milling) to the next as the feedback mechanism that also defines the time delay [3–6], and provided analytical algorithms to predict stable and unstable cutting conditions [4–16]. In 1998, approximately 50 years after Arnold's paper, Davies et al. measured period-*n* milling bifurcations, which complemented the traditional secondary (subcritical) Hopf bifurcation that had been previously studied [17]. This research led to multiple publications that modeled and predicted both the secondary Hopf and period-*n* behavior with a focus on the period-2 and period-3 cases [17–43]. Recently, Honeycutt and Schmitz presented the extended milling bifurcation diagram that revealed higher order period-*n* bifurcations at depths of cut well above the traditional stability limit [44]. They also predicted and experimentally validated period-2, −3, −6, −7, and −15 bifurcations for milling [45]. The sensitivity of period-*n* bifurcation behavior to the structural dynamics (natural frequency and damping) was studied both numerically and experimentally.

When stable machining conditions are selected, two additional considerations for high quality part manufacture are: (1) surface location error, or part geometric errors that occur due to forced vibrations; and (2) surface roughness. Surface location error (SLE) has been modeled and predicted for stable milling conditions by several authors [46–61]. In these publications, the difference between the machined surface location and the commanded location is measured and/or predicted to determine the influence of (stable) machining conditions on the error. Similarly, surface roughness has been considered as an important quality metric for machined parts since it influences fatigue, sealing performance, wear, and esthetics, for example. However, prior studies of period-*n* bifurcations (instabilities) have evaluated neither SLE nor surface roughness. The purpose of this paper is to predict and measure both quantities for stable and period-2 bifurcation behaviors. In the remaining sections of the paper, the time domain simulation algorithm is described, a numerical example is provided, the experimental setup is detailed, and numerical and experimental results are presented for SLE and surface roughness when milling under both stable and period-2 bifurcation conditions.

Time Domain Simulation

Time domain simulation enables the numerical solution of the coupled, time-delay equations of motion for milling in small time steps [59]. It is well suited to incorporating the inherent complexities of milling dynamics, including the nonlinearity that occurs if the tooth leaves the cut due to large amplitude vibrations and complicated tool geometries (incorporating runout, or different radii, of the cutter teeth, nonproportional teeth spacing, and variable helix). The simulation is based on the regenerative force, dynamic deflection model described by Smith and Tlusty [26]. As opposed to analytical stability maps that provide a global picture of the stability behavior, time domain simulation provides information regarding the local cutting force and vibration behavior for the selected cutting conditions. The simulation used in this study proceeds as follows (see Fig. 1):

(1) The instantaneous chip thickness, h(t), is determined using the vibration of the current and previous teeth at the selected tooth angle.
(2) The cutting force components in the tangential (t) and normal (n) directions are calculated using

$$\begin{aligned} \mathrm{F}_t(t) &= k_{tc} b h(t) + k_{te} b \\ \mathrm{F}_n(t) &= k_{nc} b h(t) + k_{ne} b \end{aligned} \tag{1}$$

where b is the axial depth of cut and the cutting force coefficients are identified by the subscripts t or n for direction and c or e for cutting or edge effect.
(3) The force components are used to find the new displacements by numerical solution of the differential equations of motion in the x and y directions

$$\begin{aligned} m_x\ddot{x} + c_x\dot{x} + k_x x &= \mathrm{F}_t(t)\cos\phi + \mathrm{F}_n(t)\sin\phi \\ m_y\ddot{y} + c_y\dot{y} + k_y y &= \mathrm{F}_t(t)\sin\phi - F_n(t)\cos\phi \end{aligned} \tag{2}$$

where m is the modal mass, c is the modal viscous damping coefficient, and k is the modal stiffness. The subscripts identify the direction, and multiple degrees-of-freedom in each direction can be accommodated.

[1]Corresponding author.
Manuscript received September 7, 2016; final manuscript received November 28, 2016; published online January 30, 2017. Editor: Y. Lawrence Yao.

(4) The tool rotation angle is incremented and the process is repeated.

The instantaneous chip thickness depends on the nominal, tooth angle-dependent chip thickness, the current vibration in the direction normal to the surface, and the vibration of previous teeth at the same angle. The chip thickness can be expressed using the circular tooth path approximation as

$$h(t) = f_t \sin\,\phi + n(t-\tau) - n(t) \tag{3}$$

where f_t is the commanded feed per tooth, ϕ is the tooth angle, n is the normal direction (see Fig. 1), and τ is the tooth period and represents the time delay. The tooth period is defined as

$$\tau = \frac{60}{\Omega N_t}\,(\text{sec}) \tag{4}$$

where Ω is the spindle speed in rpm and N_t is the number of teeth. The vibration in the direction of the surface normal for the current tooth depends on the x and y vibrations as well as the tooth angle according to

$$n = x\sin\phi - y\cos\phi \tag{5}$$

For the simulation, the strategy is to divide the angle of the cut into a discrete number of steps. At each small time-step, Δt, the cutter angle is incremented by the corresponding small angle, $\Delta\phi$. This approach enables convenient computation of the chip thickness for each simulation step because: (1) the possible teeth orientations are predefined; and (2) the surface created by the previous teeth at each angle may be stored. The cutter rotation

$$\Delta\phi = \frac{360}{SR}\,\text{deg} \tag{6}$$

depends on the selection of the number of steps per revolution, SR. The corresponding time-step is

$$\Delta t = \frac{60}{SR\Omega} \tag{7}$$

A vector of angles is defined to represent the potential orientations of the teeth as the cutter is rotated through one revolution of the circular tool path, $\phi = [0,\ \Delta\phi,\ 2\Delta\phi,\ 3\Delta\phi,\ \ldots,\ (SR-1)\Delta\phi]$. The locations of the teeth within the cut are then defined by referencing entries in this vector.

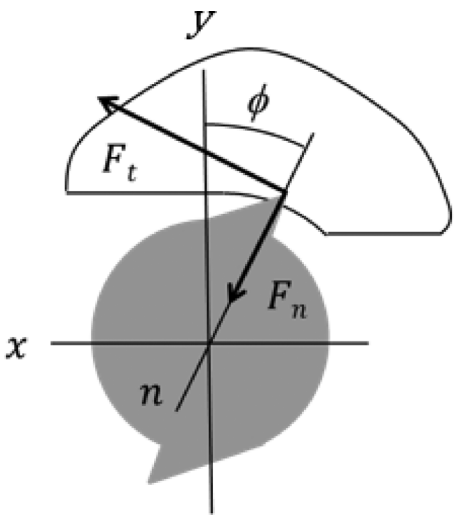

Fig. 1 Cutting force geometry. The normal and tangential direction cutting forces, F_n and F_t, are displayed. The fixed *x* (feed) and *y* directions, as well as the rotating normal direction, *n*, are also shown. The angle ϕ defines the tooth angle. The tool feed is to the right for the clockwise tool rotation and the axial depth is in the *z* direction.

In order to accommodate the helix angle for the tool's cutting edges, the tool may be sectioned into a number of axial slices. Each slice is treated as an individual straight tooth endmill with radius r, where the thickness of each slice is a small fraction, Δb, of the axial depth of cut, b. Each slice incorporates a distance delay

$$r\chi = \Delta b\tan\gamma \tag{8}$$

relative to the prior slice (nearer the cutter free end), which becomes the angular delay between slices

$$\chi = \frac{\Delta b\tan\gamma}{r} = \frac{2\Delta b\tan\gamma}{d}\,(\text{rad}) \tag{9}$$

for the rotating endmill, where d is the endmill diameter and γ is the helix angle. In order to ensure that the angles for each axial slice match the predefined tooth angles, the delay angle between slices is

$$\chi = \Delta\phi \tag{10}$$

This places a constraint on the Δb value. By substituting $\Delta\phi$ for χ and rearranging, the required slice width is

$$\Delta b = \frac{d(\Delta\phi)}{2\tan\gamma} \tag{11}$$

Once the x and y direction displacements are determined (Eq. (2)), the final spatial trajectory for each tooth is determined by summing these vibration-induced displacements with the nominal cycloidal motion of the teeth due to the combined translation and rotation. This final spatial trajectory is finally used to define the machined surface and, subsequently, to predict the SLE and surface roughness. The nominal cycloidal motion components in the x and y directions are defined in Eqs. (12) and (13), where i is the time-step index and Δf is the linear feed per time-step (see Eq. (14)).

$$x_{\text{nom}} = r\sin\,\phi + i\Delta f \tag{12}$$

$$y_{\text{nom}} = r\cos\,\phi \tag{13}$$

$$\Delta f = \frac{f_t N_t}{SR} \tag{14}$$

This simple description can be extended to include:

(1) Multiple tool modes–the x and y forces are used to calculate the acceleration, velocity, and displacement for each tool mode (represented by the modal parameters) and the results are summed in each direction.
(2) Flexible workpiece–the x and y forces are also used to determine the workpiece deflections, again by numerical integration, and the relative tool-workpiece vibration is used to calculate the instantaneous chip thickness.
(3) Runout of the cutter teeth–the chip thickness is updated by the runout of the current tooth.
(4) Unequal teeth spacing–the tooth angle vector is modified to account for the actual tooth pitch.

Numerical Example

To demonstrate stability, SLE, and surface roughness results obtained from time domain simulation, a numerical example is presented. The strategy of periodic sampling is applied to differentiate between stable machining and bifurcation behavior. The

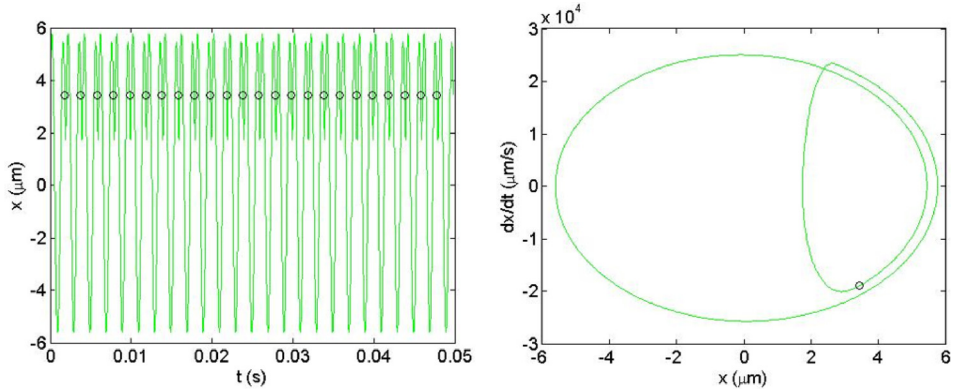

Fig. 2 (Left) Feed direction (*x*) vibration versus time with once-per-tooth sampled points (circles) for b = 0.5 mm. (Right) Poincaré map with once-per-tooth sampled points. Because the cut is stable, all sampled points appear at the same location.

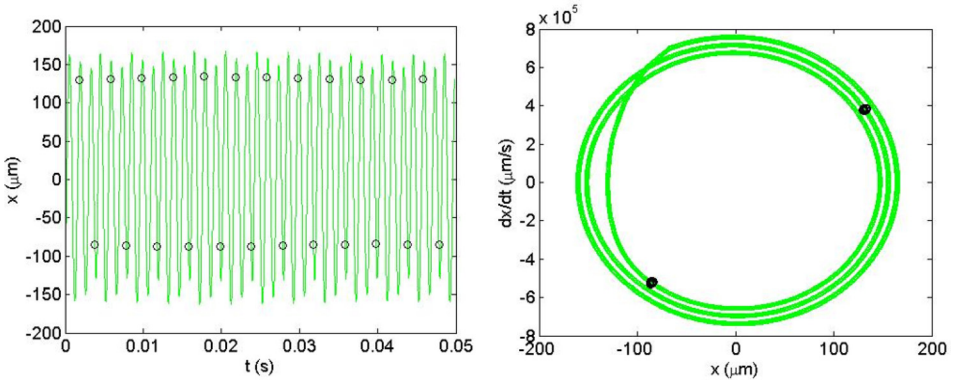

Fig. 3 (Left) Feed direction (*x*) vibration versus time with once-per-tooth sampled points (circles) for b = 2.5 mm. (Right) Poincaré map with once-per-tooth sampled points. The period-2 bifurcation behavior shows two sampled point locations. Because the solution alternates between two values, this is referred to as a flip bifurcation.

cutting conditions for the simulation are 5% radial immersion up (conventional) milling at 30,000 rpm with a feed per tooth of 0.1 mm/tooth. The 8 mm diameter, 45 deg helix, single tooth tool has symmetric dynamics with a 721 Hz natural frequency, a viscous damping ratio of 0.009, and a 4.1×10^5 N/m stiffness. The aluminum workpiece cutting force coefficients are $k_{tc} = 604 \times 10^6$ N/m^2 and $k_{nc} = 223 \times 10^6$ N/m^2 (zero edge coefficients).

The tool vibration in the feed (x) direction for an axial depth of b = 0.5 mm is displayed in Fig. 2. For this stable cut, the once-per-tooth sampled points (circles) repeat because stable cuts exhibit forced (synchronous) vibrations. The corresponding Poincaré map, which plots displacement versus velocity, is also included in Fig. 2. It is observed that a single point is obtained from the once-per-tooth (periodic) sampling. This identifies stable behavior that repeats with each tooth passage. Figure 3 shows results for b = 2.5 mm. This provides an example of period-2 behavior. In this case, the vibration repeats every other tooth passage, so two distinct points are visible in the Poincaré map. Secondary Hopf behavior is demonstrated in Fig. 4 with b = 5.0 mm. Here, the chatter frequency near the system natural frequency causes the quasi-periodic behavior and an elliptical distribution of points appears in the Poincaré map. This distribution is indicative of the traditional, secondary Hopf instability.

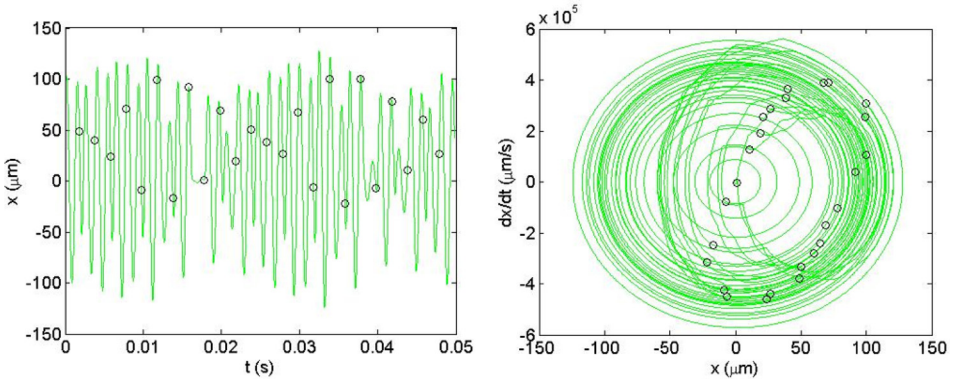

Fig. 4 (Left) Feed direction (*x*) vibration versus time with once-per-tooth sampled points (circles) for b = 5 mm. (Right) Poincaré map with once-per-tooth sampled points. The secondary Hopf instability yields an elliptical distribution of sampled points.

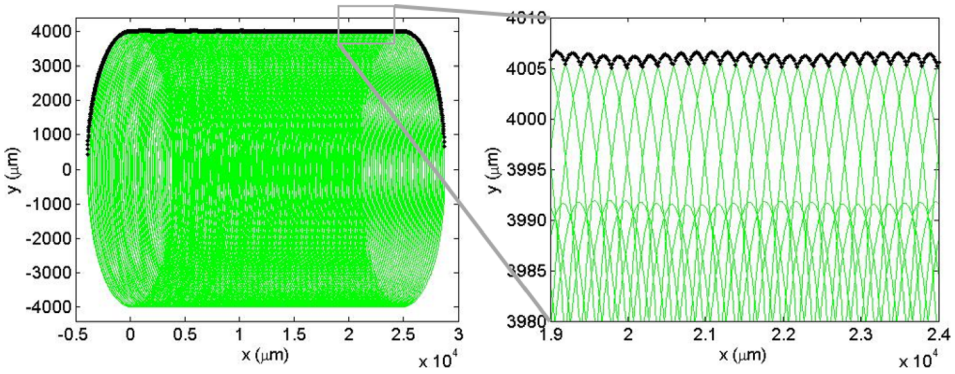

Fig. 5 (Left) Spatial trajectory of the cutter tooth for b = 2.5 mm. (Right) Magnified view of upper surface of tooth trajectory. The machined surface is defined by the points at the top of the trajectory for the up milling cut. The period-2 behavior gives upper and lower tooth paths. The upper path defines the final surface, although material is removed for each tooth passage.

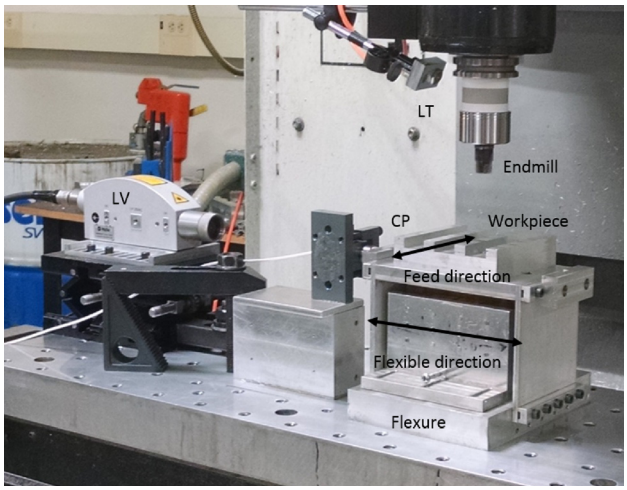

Fig. 6 Flexure-based experimental setup with laser vibrometer (LV), laser tachometer (LT), and capacitance probe (CP). The feed direction and the flexible direction for the single degree-of-freedom flexure are also identified. The setup was located on a Haas TM-1 CNC milling machine.

The spatial trajectory of the cutter tooth is displayed in Fig. 5. It includes both the nominal path and the vibrations due to the cutting force (i.e., the x solution to Eq. (2) is summed with x_{nom} from Eq. (12) and the y solution to Eq. (2) is summed with y_{nom} from Eq. (13)). Because this is up milling, the uppermost points define the machined surface (for down milling, it would be the lowermost points). The upper surface is shown in more detail in the inset. It is seen that the period-2 behavior causes the final surface to be defined by every other tooth passage. The trajectories with their apex at approximately 4006 μm produce the surface, while the alternating trajectories at approximately 3991 μm remove material, but do not affect the final surface details. In this case, the surface location error is 6 μm because the 8 mm diameter (4 mm radius) tool should leave the surface at 4000 μm. This surface is overcut by 6 μm, i.e., more material is removed than commanded. The arithmetic average surface roughness for the profile is Ra = 0.3 μm.

For the selected system dynamics, the traditional stability limit (i.e., the transition from stable to any bifurcation behavior) at 30,000 rpm is 0.77 mm. At the selected spindle speed, therefore, the optimum axial depth of cut would be 0.77 mm or less. If the 2.5 mm axial depth that resulted in period-2 behavior was chosen, a 325% increase in material removal rate would be achieved. Provided the 6 μm SLE and 0.3 μm Ra are acceptable for the selected application, this presents a compelling case for machining at the period-2 conditions.

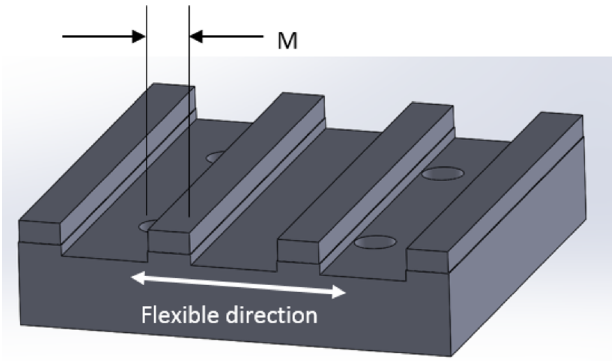

Fig. 7 The workpiece included four ribs that were initially machined to the same dimensions. The {5 mm axial depth, 2 mm radial depth} cuts were then performed on one edge at a different spindle speed for each rib. The SLE was calculated as the difference between the commanded, C, and measured, M, rib widths. The flexible direction for the flexure is identified.

Experimental Setup

The flexure-based setup displayed in Fig. 6 was used to define a physical system for simulation and testing [62,63]. The setup included a parallelogram leaf-type flexure with an aluminum workpiece mounted on top. The in-process vibration data were collected using a Polytec OFV-5000 laser vibrometer (velocity) and Lion Precision DMT20 capacitance probe (displacement).

Table 1 Spindle speeds and bifurcation behavior for experiments

Spindle speed (rpm)	Behavior
3180	Period-2
3190	Period-2
3200	Period-2
3210	Period-2
3270	Stable
3300	Stable
3330	Stable
3360	Stable
3400	Stable
3500	Stable
3600	Stable

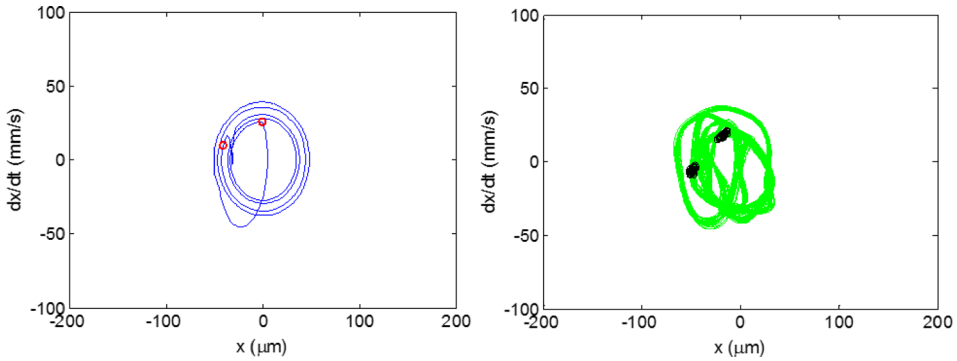

Fig. 8 Predicted (left) and measured (right) Poincaré maps for 3180 rpm. Period-2 behavior is seen. Note that x indicates the flexible direction for the flexure. The feed direction was y for these experiments.

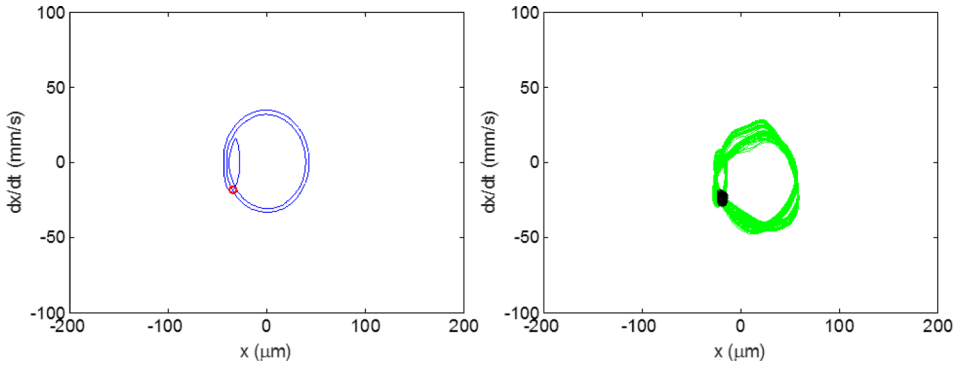

Fig. 9 Predicted (left) and measured (right) Poincaré maps for 3300 rpm. Stable behavior is seen.

Both were aligned with the flexible direction for the single degree-of-freedom flexure. Note that the feed direction is perpendicular to this flexible direction. This orientation was selected to emphasize variations in surface location error and surface finish with machining conditions. Once per tooth sampling was accomplished using a laser tachometer (LT), where the reflective target was attached to the rotating tool holder. The flexure dynamics were identified by modal testing: 125.8 Hz natural frequency, 0.0136 viscous damping ratio, and 1.75×10^6 N/m stiffness in the flexible (feed) direction. The dynamics for the 19.1 mm diameter, 0 deg helix angle tool (one insert) were symmetric: 1188 Hz natural frequency, 0.095 viscous damping ratio, and 4.24×10^7 N/m stiffness. The 6061-T6 aluminum alloy cutting force coefficients were: $k_{tc} = 770 \times 10^6$ N/m^2, $k_{nc} = 368 \times 10^6$ N/m^2, $k_{te} = 22 \times 10^3$ N/m, and $k_{ne} = 22 \times 10^3$ N/m. The up milling cutting conditions were: 5 mm axial depth, 2 mm radial depth, 0.35 mm/tooth, and variable spindle speed. Spindle speed values were selected to span from period-2 to stable cutting conditions while holding all other parameters constant. These spindle speeds and the corresponding behavior are listed in Table 1.

The workpiece geometry is presented in Fig. 7. The initial ribs were machined directly on the flexure so it could be ensured that the part was aligned with the machine axes. Low axial and radial depths were selected to minimize vibration levels and the same conditions were used to machine each rib. Prior to beginning the SLE/Ra experiments, a test workpiece was machined and the four ribs were measured on a coordinate measuring machine (CMM) to evaluate the repeatability of the starting rib dimensions (Zeiss Prismo). The mean value was 9.82 mm with a standard deviation of 2.8 μm. Given the adequate repeatability of the initial ribs, the 11 spindle speeds in Table 1 were used to machine 11 ribs (three total workpieces). All machining conditions were identical other than spindle speed.

The predicted and measured Poincaré maps for three of the 11 spindle speeds are presented in Figs. 8–10. Figure 8 displays the

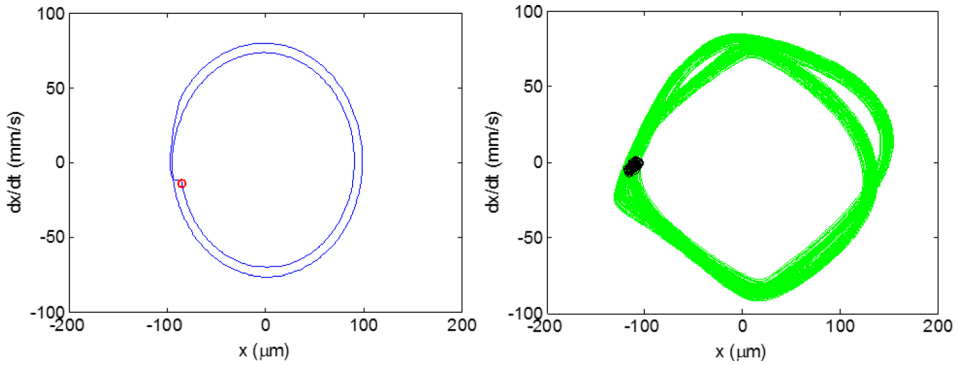

Fig. 10 Predicted (left) and measured (right) Poincaré maps for 3600 rpm. Stable behavior is seen with increased amplitude relative to 3300 rpm (Fig. 9).

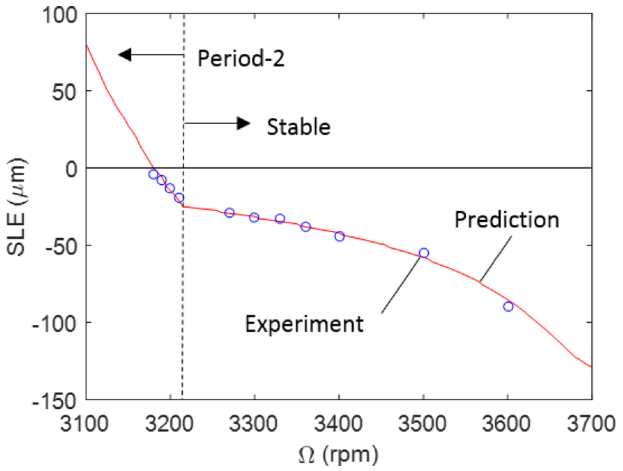

Fig. 11 SLE prediction from time domain simulation (line) and experimental results from rib cutting tests (circles). The four period-2 bifurcation tests are identified.

Table 2 Comparison of measured and predicted SLE results for rib cutting tests

Spindle speed (rpm)	Behavior	Measured SLE (μm)	Predicted SLE (μm)	Error (μm)
3180	Period-2	−4	0	−4
3190	Period-2	−8	−6	−2
3200	Period-2	−13	−15	+2
3210	Period-2	−19	−21	+2
3270	Stable	−29	−30	+1
3300	Stable	−32	−32	0
3330	Stable	−33	−35	+2
3360	Stable	−38	−38	0
3400	Stable	−44	−42	−2
3500	Stable	−55	−58	+3
3600	Stable	−90	−85	−5

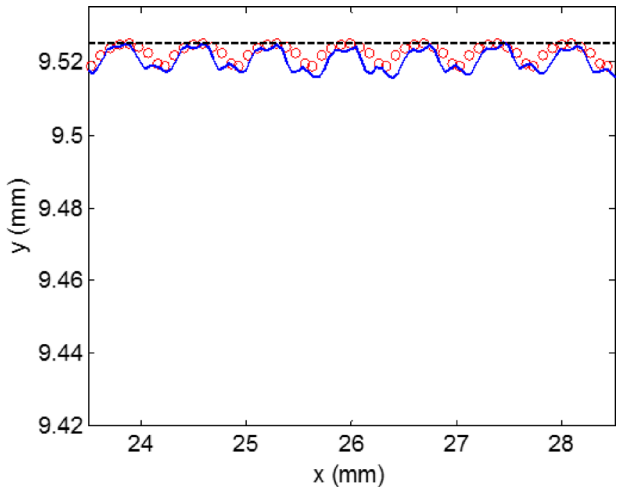

Fig. 12 Commanded surface (dashed line), CMM scan (solid line), and simulation result (circles) for 3180 rpm (period-2). These results correspond to Fig. 8.

3180 rpm results that exhibit period-2 behavior. Figures 9 and 10 both demonstrate stable behavior (3300 rpm and 3600 rpm, respectively). The vibration amplitude is larger in Fig. 10 because this spindle speed is nearer the first integer fraction of the resonant spindle speed ($(125.8 \times 60)/2 = 7548/2 = 3774$ rpm). The forced vibration amplitude is therefore increased. This would be considered a "best" spindle speed in traditional analyses because it identifies the peak of the corresponding secondary Hopf stability lobe.

The SLE results are presented in Fig. 11 and Table 2. Four tests were completed under period-2 conditions and seven were performed under stable conditions. Good agreement is observed between prediction and measurement. The average error between prediction and measurement is 0.5 μm for the 11 tests.

Figures 12–14 provide a direct comparison between the time domain simulation and the CMM surface points obtained by

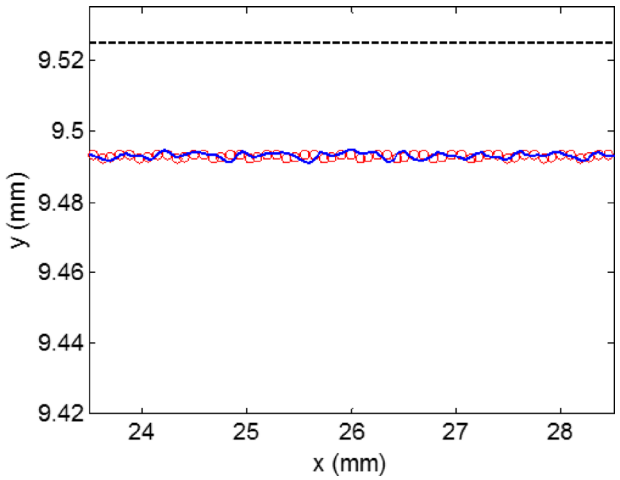

Fig. 13 Commanded surface (dashed line), CMM scan (solid line), and simulation result (circles) for 3300 rpm (stable). These results correspond to Fig. 9.

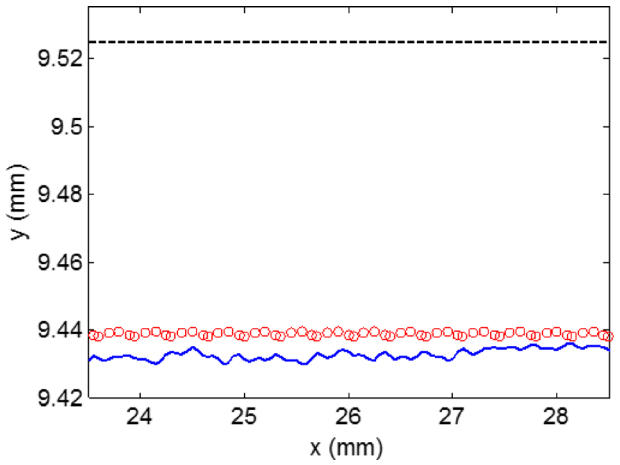

Fig. 14 Commanded surface (dashed line), CMM scan (solid line), and simulation result (circles) for 3600 rpm (stable). These results correspond to Fig. 10.

Table 3 Surface roughness results for rib cutting tests

Spindle speed (rpm)	Behavior	Ra (μm)
3180	Period-2	1.76
3190	Period-2	1.77
3200	Period-2	1.87
3210	Period-2	2.09
3270	Stable	0.28
3300	Stable	0.35
3330	Stable	0.44
3360	Stable	0.34
3400	Stable	0.39
3500	Stable	0.36
3600	Stable	0.35

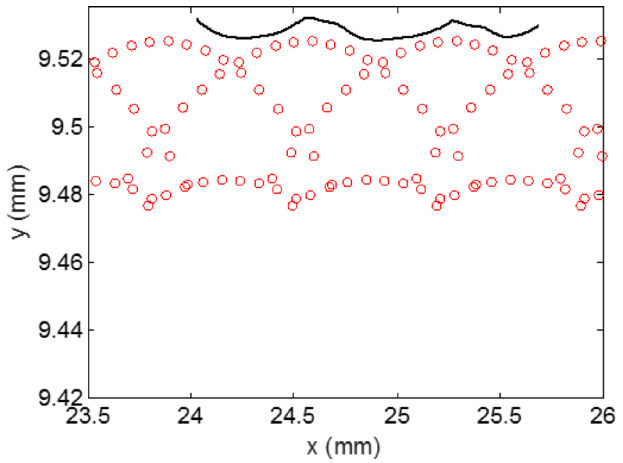

Fig. 15 Scanning white light interferometer line scan (line) and simulation results (circles) for 3180 rpm (period-2)

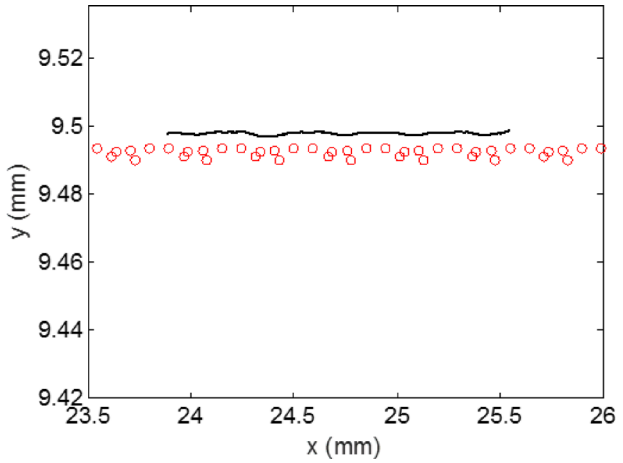

Fig. 16 Scanning white light interferometer line scan (line) and simulation results (circles) for 3300 rpm (stable)

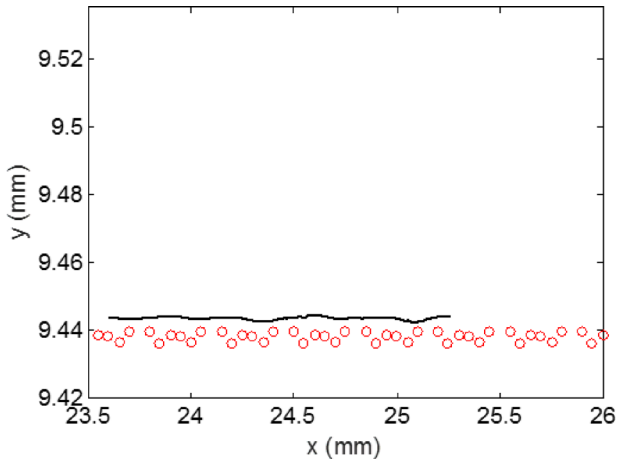

Fig. 17 Scanning white light interferometer line scan (line) and simulation results (circles) for 3600 rpm (stable)

continuous scanning along the machined surface. In these figures, the commanded surface is identified by the dashed line, the solid line is the CMM data, and the circles are the simulation results. The SLE is the difference between the commanded and actual surface and, again, good agreement is observed between simulation and measurement.

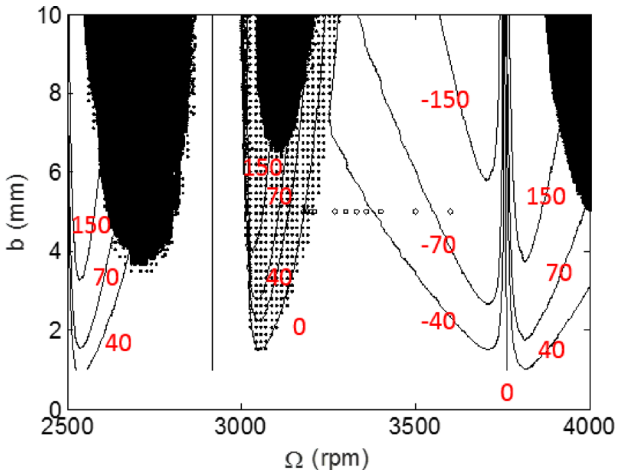

Fig. 18 Combined stability and SLE map for rib cutting process dynamics. The secondary Hopf instability is represented by the dark zone, the period-2 behavior is identified by the dotted zone, and the SLE is given by the contours (i.e., lines of constant SLE).

The surface roughness was also measured using a scanning white light interferometer (ZeGage, Zygo Corporation, Middlefield, CT). These results are presented in Table 3, where the Ra values were calculated from a line scan at the midpoint of the axial depth of cut extracted from the surface topography. The Ra is clearly larger for the period-2 conditions, where every other tool passage defines the surface roughness. The mean Ra for the period-2 conditions (four tests, 1.87 μm) is 5.2 times larger than the mean Ra for the stable conditions (seven tests, 0.36 μm).

The predicted and measured surface profiles are compared in Figs. 15–17. The change in cusp height and spacing between the period-2 (Fig. 15) and stable (Figs. 16 and 17) results is clearly seen.

The stability and SLE information are combined in Fig. 18. In Fig. 18, the dark area represents secondary Hopf instability, the dotted area identifies the period-2 bifurcations, and the contour lines give the SLE as a function of spindle speed (horizontal axis) and axial depth of cut (vertical axis). Zero SLE is seen near the traditional best speed of 3774 rpm. However, a steep gradient for small changes in spindle speed is also seen near this speed (i.e., the zero SLE contour is vertical). A zero SLE contour is also observed within the period-2 zone. Interestingly, the SLE gradient is not as steep within the period-2 zone as it is near the best speed at 3774 rpm. This also supports the possibility of producing acceptable parts under period-2 bifurcation machining conditions.

Conclusions

Surface location error and surface roughness predictions were completed using time domain simulation for both stable and period-2 milling conditions. The predictions were compared to experiment using a flexure-based platform with displacement and velocity metrology. It was observed that the simulation accurately predicted the milling performance using: (1) Poincaré maps, which plot the displacement versus velocity and are used to identify period-2 behavior via periodic sampling; (2) surface location error measurements completed using a coordinate measuring machine; and (3) surface roughness measurements carried out using a scanning white light interferometer. It was shown that the surface location error for period-2 (unstable) behavior follows similar trends observed for (stable) forced vibration, so zero or low error conditions may be selected even for period-2 bifurcation conditions. The surface roughness for the period-2 instability was seen to be larger than for stable conditions, although the final surface was still periodic. This increase in surface roughness occurs because the surface is defined by every other tooth passage and the apparent feed per tooth is increased.

Acknowledgment

This material is based on work supported by the National Science Foundation under Grant No. CMMI-1561221.

References

[1] Arnold, R. N., 1946, "The Mechanism of Tool Vibration in the Cutting of Steel," Proc. Inst. Mech. Eng., **154**(1), pp. 261–284.
[2] Doi, S., and Kato, S., 1956, "Chatter Vibration of Lathe Tools," Trans. ASME, **78**, pp. 1127–1134.
[3] Tobias, S. A., and Fishwick, W., 1958, "The Chatter of Lathe Tools Under Orthogonal Cutting Conditions," Trans. ASME, **80**, pp. 1079–1088.
[4] Tlusty, J., and Polacek, M., 1963, "The Stability of Machine Tools Against Self-Excited Vibrations in Machining," ASME International Research in Production Engineering Conference, Pittsburgh, PA, pp. 465–474.
[5] Tobias, S. A., 1965, *Machine Tool Vibration*, Wiley, New York.
[6] Merritt, H. E., 1965, "Theory of Self-Excited Machine-Tool Chatter," ASME J. Eng. Ind., **87**(4), pp. 447–454.
[7] Shridar, R., Hohn, R. E., and Long, G. W., 1968, "A General Formulation of the Milling Process Equation," ASME J. Eng. Ind., **90**(2), pp. 317–324.
[8] Hohn, R. E., Shridar, R., and Long, G. W., 1968, "A Stability Algorithm for a Special Case of the Milling Process: Contribution to Machine Tool Chatter Research—6," ASME J. Eng. Ind., **90**(2), pp. 326–329.
[9] Shridar, R., Hohn, R. E., and Long, G. W., 1968, "A Stability Algorithm for the General Milling Process: Contribution to Machine Tool Chatter Research—7," ASME J. Eng. Ind., **90**(2), pp. 330–334.
[10] Hanna, N. H., and Tobias, S. A., 1974, "A Theory of Nonlinear Regenerative Chatter," ASME J. Eng. Ind., **96**(1), pp. 247–255.
[11] Tlusty, J., and Ismail, F., 1981, "Basic Non-Linearity in Machining Chatter," Ann. CIRP, **30**(1), pp. 299–304.
[12] Tlusty, J., and Ismail, F., 1983, "Special Aspects of Chatter in Milling," ASME J. Vib., Stress Reliab. Des., **105**(1), pp. 24–32.
[13] Tlusty, J., 1985, "Machining Dynamics," *Handbook of High-Speed Machining Technology*, R. I. King, ed., Chapman and Hall, New York, pp. 48–153.
[14] Tlusty, J., 1986, "Dynamics of High-Speed Milling," ASME J. Eng. Ind., **108**(2), pp. 59–67.
[15] Minis, I., and Yanusevsky, R., 1993, "A New Theoretical Approach for Prediction of Chatter in Milling," ASME J. Eng. Ind., **115**(1), pp. 1–8.
[16] Altintas, Y., and Budak, E., 1995, "Analytical Prediction of Stability Lobes in Milling," Ann. CIRP, **44**(1), pp. 357–362.
[17] Davies, M. A., Dutterer, B. S., Pratt, J. R., and Schaut, A. J., 1998, "On the Dynamics of High-Speed Milling With Long, Slender Endmills," Ann. CIRP, **47**(1), pp. 55–60.
[18] Moon, F. C., and Kalmár-Nagy, T., 2001, "Nonlinear Models for Complex Dynamics in Cutting Materials," Philos. Trans. R. Soc., A, **359**(1781), pp. 695–711.
[19] Davies, M. A., Pratt, J. R., Dutterer, B. S., and Burns, T. J., 2000, "The Stability of Low Radial Immersion Milling," Ann. CIRP, **49**(1), pp. 37–40.
[20] Moon, F. C., 1994, "Chaotic Dynamics and Fractals in Material Removal Processes," *Nonlinearity and Chaos in Engineering Dynamics*, J. Thompson, and S. Bishop, ed., Wiley, New York, pp. 25–37.
[21] Bukkapatnam, S., Lakhtakia, A., and Kumara, S., 1995, "Analysis of Senor Signals Shows Turning on a Lathe Exhibits Low-Dimensional Chaos," Phys. Rev., E, **52**(3), pp. 2375–2387.
[22] Stépán, G., and Kalmár-Nagy, T., 1997, "Nonlinear Regenerative Machine Tool Vibrations," Proceedings of the ASME Design Engineering Technical Conference on Vibration and Noise, Sacramento, CA, Sept. 14–17.
[23] Nayfey, A., Chin, C., and Pratt, J., 1998, "Applications of Perturbation Methods to Tool Chatter Dynamics," *Dynamics and Chaos in Manufacturing Processes*, F. C. Moon, ed., Wiley, New York, pp. 193–213.
[24] Minis, I., and Berger, B. S., 1998, "Modelling, Analysis, and Characterization of Machining Dynamics," *Dynamics and Chaos in Manufacturing Processes*, F. C. Moon, ed., Wiley, New York, pp. 125–163.
[25] Moon, F. C., and Johnson, M., 1998, "Nonlinear Dynamics and Chaos in Manufacturing Processes," *Dynamics and Chaos in Manufacturing Processes*, F. C. Moon, ed., Wiley, New York, pp. 3–32.
[26] Smith, K. S., and Tlusty, J., 1991, "An Overview of Modeling and Simulation of the Milling Process," ASME J. Eng. Ind., **113**(2), pp. 169–175.
[27] Campomanes, M. L., and Altintas, Y., 2003, "An Improved Time Domain Simulation for Dynamic Milling at Small Radial Immersions," ASME J. Manuf. Sci. Eng., **125**(3), pp. 416–422.
[28] Zhao, M. X., and Balachandran, B., 2001, "Dynamics and Stability of Milling Process," Int. J. Solids Struct., **38**(10–13), pp. 2233–2248.
[29] Davies, M. A., Pratt, J. R., Dutterer, B., and Burns, T. J., 2002, "Stability Prediction for Low Radial Immersion Milling," ASME J. Manuf. Sci. Eng., **124**(2), pp. 217–225.
[30] Mann, B. P., Insperger, T., Bayly, P. V., and Stépán, G., 2003, "Stability of up-Milling and Down-Milling, Part 2: Experimental Verification," Int. J. Mach. Tools Manuf., **43**(1), pp. 35–40.
[31] Mann, B. P., Insperger, T., Bayly, P. V., and Stépán, G., 2003, "Stability of up-Milling and Down-Milling—Part 1: Alternative Analytical Methods," Int. J. Mach. Tools Manuf., **43**(1), pp. 25–34.
[32] Insperger, T., Stépán, G., Bayly, P. V., and Mann, B. P., 2003, "Multiple Chatter Frequencies in Milling Processes," J. Sound Vib., **262**(2), pp. 333–345.
[33] Insperger, T., and Stépán, G., 2004, "Vibration Frequencies in High-Speed Milling Processes or A Positive Answer to Davies, Pratt, Dutterer, and Burns," ASME J. Manuf. Sci. Eng., **126**(3), pp. 481–487.
[34] Mann, B. P., Bayly, P. V., Davies, M. A., and Halley, J. E., 2004, "Limit Cycles, Bifurcations, and Accuracy of the Milling Process," J. Sound Vib., **277**(1–2), pp. 31–48.
[35] Merdol, S. D., and Altintas, Y., 2004, "Multi Frequency Solution of Chatter Stability for Low Immersion Milling," ASME J. Manuf. Sci. Eng., **126**(3), pp. 459–466.
[36] Govekar, E., Gradišek, J., Kalveram, M., Insperger, T., Weinert, K., Stepan, G., and Grabec, I., 2005, "On Stability and Dynamics of Milling at Small Radial Immersion," Ann. CIRP, **54**(1), pp. 357–362.
[37] Gradišek, J., Kalveram, M., Insperger, T., Weinert, K., Stépán, G., Govekar, E., and Grabec, I., 2005, "On Stability Prediction for Milling," Int. J. Mach. Tools Manuf., **45**(7–8), pp. 769–781.
[38] Mann, B. P., Garg, N. K., Young, K. A., and Helvey, A. M., 2005, "Milling Bifurcations From Structural Asymmetry and Nonlinear Regeneration," Nonlinear Dyn., **42**(4), pp. 319–337.
[39] Stépán, G., Szalai, R., Mann, B. P., Bayly, P. V., Insperger, T., Gradisek, J., and Govekar, E., 2005, "Nonlinear Dynamics of High-Speed Milling–Analyses, Numerics, and Experiments," ASME J. Vib. Acoust., **127**(2), pp. 197–203.
[40] Zatarain, M., Muñoa, J., Peigné, G., and Insperger, T., 2006, "Analysis of the Influence of Mill Helix Angle on Chatter Stability," Ann. CIRP, **55**(1), pp. 365–368.
[41] Insperger, T., Munoa, J., Zatarain, M. A., and Peigné, G., 2006, "Unstable Islands in the Stability Chart of Milling Processes Due to the Helix Angle," CIRP 2nd International Conference on High Performance Cutting, Vancouver, Canada, June 12–13, Vancouver, BC, Canada, pp. 12–13.
[42] Patel, B. R., Mann, B. P., and Young, K. A., 2008, "Uncharted Islands of Chatter Instability in Milling," Int. J. Mach. Tools Manuf., **48**(1), pp. 124–134.
[43] Moradi, H., Vossoughi, G., and Movahhedy, M., 2014, "Bifurcation Analysis of Nonlinear Milling Process With Tool Wear and Process Damping: Sub-Harmonic Resonance Under Regenerative Chatter," Int. J. Mech. Sci., **85**, pp. 1–19.
[44] Honeycutt, A., and Schmitz, T., 2015, "The Extended Milling Bifurcation Diagram," Proc. Manuf., **1**, pp. 466–476.
[45] Honeycutt, A., and Schmitz, T., 2016, "A Numerical and Experimental Investigation of Period-*n* Bifurcations in Milling," ASME J. Manuf. Sci. Eng., **139**(1), p. 011003.
[46] Kline, W., DeVor, R., and Shareef, I., 1982, "The Prediction of Surface Accuracy in End Milling," ASME J. Eng. Ind., **104**(3), pp. 272–278.
[47] Kline, W., DeVor, R., and Lindberg, J., 1982, "The Prediction of Cutting Forces in End Milling With Application to Cornering Cuts," Int. J. Mach. Tool Des. Res., **22**(1), pp. 7–22.
[48] Tlusty, J., 1985, "Effect of End Milling Deflections on Accuracy," *Handbook of High Speed Machining Technology*, R. I. King, ed., Chapman and Hall, New York, pp. 140–153.
[49] Sutherland, J., and DeVor, R., 1986, "An Improved Method for Cutting Force and Surface Error Prediction in Flexible End Milling Systems," ASME J. Eng. Ind., **108**(4), pp. 269–279.
[50] Montgomery, D., and Altintas, Y., 1991, "Mechanism of Cutting Force and Surface Generation in Dynamic Milling," ASME J. Eng. Ind., **113**(2), pp. 160–168.
[51] Altintas, Y., Montgomery, D., and Budak, E., 1992, "Dynamic Peripheral Milling of Flexible Structures," ASME J. Eng. Ind., **114**(2), pp. 137–145.
[52] Tarng, Y., Liao, C., and Li, H., 1994, "A Mechanistic Model for Prediction of the Dynamics of Cutting Forces in Helical End Milling," Int. J. Model. Simul., **14**(2), pp. 92–97.
[53] Schmitz, T., and Ziegert, J., 1999, "Examination of Surface Location Error Due to Phasing of Cutter Vibrations," Prec. Eng., **23**(1), pp. 51–62.
[54] Altintas, Y., 2000, *Manufacturing Automation*, Cambridge University Press, Cambridge, UK.
[55] Mann, B. P., Bayly, P. V., Davies, M. A., and Halley, J. E., 2004, "Limit Cycles, Bifurcations, and Accuracy of the Milling Process," J. Sound Vib., **277**(1–2), pp. 31–48.
[56] Schmitz, T., Couey, J., Marsh, E., Mauntler, N., and Hughes, D., 2007, "Runout Effects in Milling: Surface Finish, Surface Location Error, and Stability," Int. J. Mach. Tools Manuf., **47**(5), pp. 841–851.
[57] Yun, W.-S., Ko, J., Cho, D.-W., and Ehmann, K., 2002, "Development of a Virtual Machining System—Part 2: Prediction and Analysis of a Machined Surface Error," Int. J. Mach. Tools Manuf., **42**(15), pp. 1607–1615.
[58] Schmitz, T., and Mann, B., 2006, "Closed-Form Solutions for Surface Location Error in Milling," Int. J. Mach. Tools Manuf., **46**(12–13), pp. 1369–1377.
[59] Schmitz, T., and Smith, K. S., 2009, *Machining Dynamics: Frequency Response to Improved Productivity*, Springer, New York.
[60] Dombovari, Z., and Stépán, G., 2015, "On the Bistable Zone of Milling Processes," Philos. Trans. R. Soc., A, **373**(2051), p. 20140409.
[61] Bachrathy, D., Munoa, J., and Stépán, G., 2016, "Experimental Validation of Appropriate Axial Immersions for Helical Mills," Int. J. Adv. Manuf. Technol., **84**(5), pp. 1295–1302.
[62] Mann, B. P., Insperger, T., Bayly, P. V., and Stépán, G., 2003, "Stability of Up-Milling and Down-Milling—Part 2: Experimental Verification," Int. J. Mach. Tools Manuf., **43**(1), pp. 35–40.
[63] Ransom, T., Honeycutt, A., and Schmitz, T., 2016, "A New Tunable Dynamics Platform for Milling Experiments," Prec. Eng., **44**, pp. 252–256.